Available online at www.sciencedirect.com
SCIENCE DIRECT®
International Journal of Heat and Mass Transfer 48 (2005) 3945–3956
International Journal of HEAT and MASS TRANSFER
www.elsevier.com/locate/ijhmt

Microfluidic exergy loss in a non-polarized thermomagnetic field

G.F. Naterer *, O.B. Adeyinka

Department of Mechanical and Manufacturing Engineering, University of Manitoba, 15 Gillson Street, Winnipeg, Manitoba, Canada R3T 2N2

Received 11 November 2004; received in revised form 15 April 2005
Available online 28 June 2005

Abstract

In this article, exergy losses of fluid motion in a microchannel are investigated. Thermal, friction and electromagnetic irreversibilities contribute to the total rate of exergy destruction. Additional input power from the externally applied electric field is needed to overcome these irreversibilities and deliver specified rates of mass and heat flow through the microchannel. Different cases of steady-state heat transfer in a non-polarized electromagnetic field are considered. Predicted results of fluid velocity, exergy destruction and optimal Reynolds number are presented and compared successfully against past data and measurements involving exergy destruction. It is shown that exergy destruction increases with stronger magnetic fields and wider microchannels. Furthermore, the optimal Reynolds number (minimizing the rate of exergy destruction) increases at lower microchannel aspect ratios.

1. Introduction

Microfluidic friction and pressure losses have significance in the achievement of various technological goals involving microdevices, i.e., microchannel cooling, biomedical separation devices and others [1]. Embedded surface microchannels utilize slip-flow conditions to reduce wall friction and entropy production, while improving thermal effectiveness of convective heat exchange with EBSM (entropy-based surface micro-profiling [2,3]). Furthermore, they may affect the characteristics of boundary layer separation, when the near-wall pressure gradient changes along their converging/diverging profiles [4]. In these applications, fluid friction and pressure losses within a microchannel are important issues for design purposes. This article considers how electromagnetic fields affect wall friction and heat exchange, particularly regarding their characterization by exergy losses within a microchannel.

Manipulating different charge patterns along the walls of a microchannel affects the speed and direction of electrokinetic flow. A charged surface of a microchannel wall will attract ions of the opposite charge in the surrounding fluid. The resulting spatial gradient of ions leads to an EDL (electric double layer). This EDL contains an immobile inner layer and an outer layer, which can be affected by an external electric field. This article develops a predictive model of microfluidic motion, which includes electromagnetic forces in the axial momentum equation.

Recent studies have shown that microfluidic transport between parallel walls affects the surface free energy

* Corresponding author. Tel.: +1 204 474 9805; fax: +1 204 275 7507.
E-mail address: natererg@cc.umanitoba.ca (G.F. Naterer).

0017-9310/$ - see front matter © 2005 Elsevier Ltd. All rights reserved.
doi:10.1016/j.ijheatmasstransfer.2005.04.012

Nomenclature

a	half-width of microchannel
b	half-height of microchannel
B	magnetic field strength
c_p	specific heat
C	electromagnetic coefficient
D_h	hydraulic diameter
E	electric field (vector)
f	friction factor
h	enthalpy
H_e	electric field strength
i	current density
k	thermal conductivity
K	load factor
L	length of microchannel
$\dot{m}$	mass flow rate
M	Hartmann number
N	thermomagnetic number
p	pressure
$\dot{P}_s$	entropy production rate
Pr_m	magnetic Prandtl number
q	heat flux
Re	Reynolds number
s	specific entropy
t	time
T	temperature
v'''	specific volume
u, v	velocity components
x, y, z	Cartesian coordinates
X	exergy

Greek symbols

β	microchannel aspect ratio (b/a)
μ	dynamic viscosity
θ	non-dimensional temperature
ρ	density
σ_e	electrical conductivity
τ	viscous stress

Subscripts

b	bulk (average)
d	destruction
opt	optimum
w	wall
x, y, z	Cartesian coordinates

inside a microchannel network [5]. Zhao et al. [5] have reported that the maximum pressure within a hydrophilic pathway can be determined by the surface free energy, contact angle of the liquid and the microchannel depth. The fluid motion remains confined within the pathways, provided the fluid pressure remains below a critical value.

In heat transfer applications, the large surface area to volume ratio of microchannels allows large heat fluxes to be transferred in ultra-compact and efficient heat exchangers. Ng and Tan [6] have developed a 3-D finite volume model of fluid motion within rectangular microchannels based on the Navier–Stokes equations, including the electric double layer along the walls. Electromagnetic effects of the EDL are modeled as an additional body force and source term in the momentum equation. Variations of the electric potential are predicted by the Poisson–Boltzmann equation. The predictions analyze the effects of varying Reynolds numbers and electric potentials on the thermal effectiveness. Cho et al. [7] have developed a condition for EWOD (electrowetting on dielectric) in microfluidic motion through parallel-plate channels. In these problems, microfluidic transport is affected by the channel gap size, droplet size and the contact angle change in EWOD.

The archival literature gives conflicting opinions regarding the apparent viscosity of fluids in microchannels. This debate involves whether the apparent (required or measured) viscosity of the microchannel flow equals the bulk viscosity at large distances away from the wall. For thin films, Israelachvili [8] reported values of apparent viscosity to be much larger than the bulk viscosity. Migun and Prokhorenko [9] reported that the apparent viscosity increases for capillaries smaller than a micron in diameter. However, other researchers [10] have reported that the apparent and bulk viscosities are nearly equal for flows in capillaries. In these studies, the bulk viscosity is generally determined from classical thermodynamics, whereby curve fits of measured data to interpolating polynomials are used to estimate the variations of viscosity with temperature and pressure.

In contrast, other authors have predicted viscosity and thermal conductivity from methods of statistical thermodynamics, based on a velocity or temperature distribution function that can accommodate the effects of intermolecular interactions [11]. Avsec [12,13] applies statistical methods to include translational, rotational, vibrational and electron excitation effects on property evaluation for liquids. Gad-el-Hak [1] has extended such derivations to viscous processes in microfluidic transport by outlining a Knudsen number dependence in the velocity distribution function. For small Knudsen numbers, the distribution function can be expanded as a power series in terms of the Knudsen number. This dependence becomes negligible at small Knudsen numbers in macro-scale flows, so that viscosity only depends on two variables (pressure and temperature) for such flows.

Pfahler et al. [14,15] measured the friction factor of liquids (isopropyl alcohol, silicon oil) and gases (nitrogen, helium) flowing through microchannels etched in silicon. The liquid flow rate was measured as a function of channel size, pressure drop and type of fluid. It was observed that the fluid's apparent viscosity was smaller than values predicted for macro-scale flows. Although some speculation regarding rarefaction and thermal effects was noted, the authors "do not have a satisfactory theoretical explanation for the phenomena observed" [15]. A trend of decreasing friction constant with decreasing Reynolds number was observed, although macro-scale theory predicts a constant friction factor for laminar flow.

Exergy destruction includes both friction and thermal irreversibilities. In addition, past studies have investigated irreversibilities due to phase change in multiphase problems [16–19], which can be tracked spatially by methods of CFD [20]. Camberos [21] predicted electromagnetic irreversibilities with CFD in aircraft design. The main objectives of this article involve showing that exergy losses of electromagnetic irreversibilities provide useful insight regarding fluid friction, pressure losses and near-wall velocity profiles in microchannels. In this article, an analytical formulation of electromagnetic exergy losses is developed for microchannel applications. Predicted results for electrohydrodynamic motion in rectangular channels are compared successfully against past data.

2. Formulation of fluid flow

During electrokinetic flow in microchannels, the charged surface of a microchannel wall may attract ions of the opposite charge in the surrounding fluid. As mentioned previously, the resulting spatial gradient of ions near the wall leads to an EDL (Electric Double Layer; see Fig. 1). This EDL contains an inner layer (immobile) and a mobile outer layer, which can be appreciably affected by an externally applied electric field. The EDL reduces the liquid velocity and affects the frictional losses. For example, the friction coefficient increases when the ionic concentration of an aqueous solution decreases. In this article, spatial changes of the electromagnetic forces on the fluid will be considered and modeled as a source term in the axial momentum equation.

Consider a non-polarized thermomagnetic field that is exerted on a steady-state fully developed flow in a rectangular microchannel (see Fig. 1). The separation between walls ($2b$) is assumed to be much larger than the distance of $2a$. An electromagnetic wave is polarized if the electric field vibrates in only one direction. In this article, the electromagnetic waves transmitted through the microchannel are non-polarized, since the applied electric field is assumed to vibrate in many directions simultaneously. Polarization is a phenomenon associated with transverse electromagnetic waves. Longitudinal waves, such as sound, cannot be polarized. Ordinary light is another example of non-polarized electromagnetic waves, since the electric field vibrates in multiple directions at the same time. The non-polarized waves traveling in the y-direction of the microchannel are a superposition of many waves. For each wave, the electric field is perpendicular to the y-axis and the angle it makes with the x-axis varies for different waves. For polarized waves, the angle that the electric field makes with the x-axis would be unique.

The general form of the momentum equation for electrohydrodynamic flow is

$$\rho \frac{\partial \vec{v}}{\partial t} + \rho \vec{v} \cdot \nabla \vec{v} = -\nabla p + \nabla \cdot (\mu \nabla \vec{v}) + \vec{i} \times \vec{B} \qquad (1)$$

where the last term represents the electromagnetic force and i and B refer to the current density and magnetic field strength, respectively. For steady-state flow in a

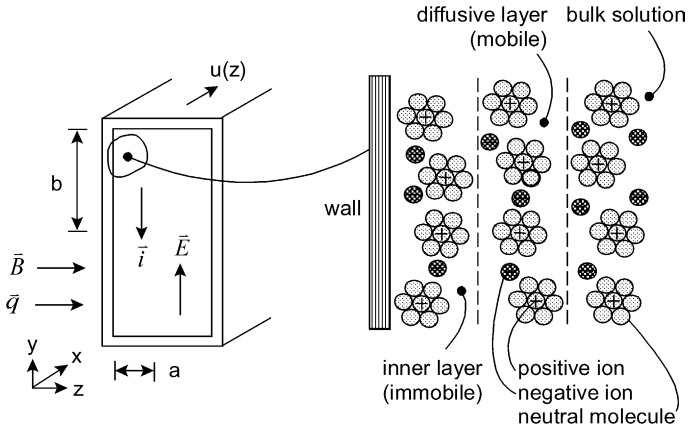

Fig. 1. Schematic of electrohydrodynamic flow with an electric double layer.

microchannel at small Reynolds numbers (see Fig. 1), the transient and inertia terms can be neglected and the reduced form of the momentum equation becomes

$$0 = -\nabla p + \nabla \cdot (\mu \nabla \vec{v}) + \vec{i} \times \vec{B} \tag{2}$$

The fluid velocity, magnetic field and current density fields are assumed as orthogonal. As a result, the net force exerted by the magnetic field on the fluid is perpendicular to the direction of the fluid velocity. Positive charges accelerate in the direction of the electric field and negative charges accelerate in a direction opposite to the electric field.

Also, the applied electric field is non-polarized and the cross-product of the electromagnetic source term in Eq. (2) can be simplified to give the following x-momentum equation:

$$0 = -\frac{\mathrm{d}p}{\mathrm{d}x} + \mu \frac{\mathrm{d}^2 u}{\mathrm{d}z^2} + i_y B_z \tag{3}$$

The terms represent pressure, viscous and electromagnetic forces on the liquid. Using Ohm's Law to express the current density in terms of fluid velocity yields

$$\mu \frac{\mathrm{d}^2 u}{\mathrm{d}z^2} + \sigma_e B_z^2 u = \frac{\mathrm{d}p}{\mathrm{d}x} \tag{4}$$

where σ_e and B_z refer to the electrical conductivity and magnetic field strength (z-direction), respectively. For fully developed flow in the microchannel, the pressure gradient becomes constant and independent of the magnetic field strength.

In terms of the Hartmann number, M (where $M = aB_z\sqrt{\sigma_e/\mu}$), Eq. (4) becomes

$$\mu \frac{\mathrm{d}^2 u}{\mathrm{d}z^2} - \left(\frac{M^2 \mu}{a^2}\right) u = \frac{\mathrm{d}p}{\mathrm{d}x} \tag{5}$$

Applying no-slip boundary conditions at $z = a$ and $z = -a$ (note: origin of coordinates at mid-plane of Fig. 1), the analytical solution of Eq. (5) becomes

$$u(z) = \frac{a^2(\mathrm{d}p/\mathrm{d}x)}{\mu M^2}\left(\frac{\cosh(Mz/a)}{\cosh M} - 1\right) \tag{6}$$

The mean velocity within the microchannel can be determined as follows:

$$u_b = \frac{1}{2a}\int_{-a}^{a} u(z)\mathrm{d}z \tag{7}$$

Substituting the velocity profile and performing the spatial integration,

$$u_b = \frac{a^2(\mathrm{d}p/\mathrm{d}x)}{\mu M^2}\left(\frac{\sinh M}{M\cosh M} - 1\right) \tag{8}$$

After non-dimensionalizing the z-coordinate ($z^* = z/a$) and velocity ($u^* = u/u_b$),

$$u^* = \frac{M\cosh M - M\sinh(Mz^*)}{M\cosh M - \sinh M} \tag{9}$$

With a Large Hartmann number Approximation (*LHA* model), the velocity becomes

$$u^* = 1 - \mathrm{e}^{M(z^*-1)} \tag{10}$$

Furthermore, the friction coefficient is defined as

$$c_f = \frac{\tau_w}{\rho u_b^2/2} = \frac{\mu(\mathrm{d}u^*/\mathrm{d}z^*)_{\pm 1}}{\rho u_b a/2} \tag{11}$$

Differentiating the previous velocity profile and evaluating the result along the bottom wall,

$$c_f = \frac{8\mathrm{e}^{-M}}{M/Re} \tag{12}$$

where Re is the Reynolds number, based on the half-width of the microchannel.

3. Convective heat transfer formulation

For convective heat transfer within the microchannel, the transient, inertial and streamwise conduction terms can be neglected for small Reynolds numbers at steady state. Then the reduced form of the energy equation becomes

$$k\frac{\mathrm{d}^2 T}{\mathrm{d}z^2} + \mu\left(\frac{\mathrm{d}u}{\mathrm{d}z}\right)^2 + \frac{i_y^2}{\sigma_e} = 0 \tag{13}$$

Define the following non-dimensional temperature, θ, and electromagnetic coefficient, C

$$\theta(z^*) = \frac{k(T - T_w)}{\mu u_b^2} \tag{14}$$

$$C = M(K-1)\cosh M - K\sinh M \tag{15}$$

where K represents a non-dimensional load factor (ratio of the applied electric field strength to the product of the mean velocity, u_b, and magnetic field strength).

In terms of the non-dimensional variables, the energy equation becomes

$$\frac{\mathrm{d}^2\theta}{\mathrm{d}z^{*2}} = -\left(\frac{\mathrm{d}u^*}{\mathrm{d}z^*}\right)^2 - i_y^{*2} \tag{16}$$

where

$$i_y^* = \frac{i_y}{u_b\sqrt{\sigma_e \mu}/a} \tag{17}$$

Eq. (16) can be solved analytically, based on the velocity solution from the momentum equation. From Ohm's Law, the current can be expressed in terms of the velocity as follows:

$$i_y^* = -M(K - u^*) \tag{18}$$

Thus, the energy equation becomes a second-order differential equation with known functions of z^* on the right side of Eq. (16), based on the velocity solution from the momentum equation.

4. Formulation of exergy losses

In previous sections, the streamwise (x-direction) gradients of velocity and viscous stress were neglected, so the reduced form of the exergy transport equation can be expressed as [22]:

$$\frac{DX}{Dt} = \frac{\partial}{\partial z}\left[k\left(1-\frac{T_0}{T}\right)\frac{\partial T}{\partial z}\right] + \frac{\partial(u\tau)}{\partial z} - \dot{X}_d \tag{19}$$

where DX/Dt refers to the total convective derivative of exergy, X. Also, the rate of exergy destruction, $\dot{X}_d$, can be represented by the reference temperature, T_0, multiplied by the local entropy production rate, $\dot{P}_s$. As a result, the local rate of entropy production is needed to calculate the exergy destroyed by friction, thermal and electromagnetic irreversibilities.

This rate of entropy production within the microchannel can be determined from the energy, entropy and Gibbs equations as follows (see Fig. 2):

$$\dot{m}\,dh = q'\,dx + \left(\frac{i_y^2}{\sigma}\right)2a\cdot 2b\cdot dx \tag{20}$$

$$d\dot{P}_s = \dot{m}\,ds - \frac{q'dx}{T+\Delta T} \geqslant 0 \tag{21}$$

$$dh = T\,ds + v'''dp \tag{22}$$

In these equations, h, q', s, v''' and $\dot{P}_s$ refer the fluid enthalpy, heat flow (per unit length), specific entropy, specific volume and entropy production rate, respectively.

The mass flow rate can be written in terms of the microchannel aspect ratio, β, as follows,

$$\dot{m} = \rho u_b(4ab) = \rho u_b 4\beta a^2 \tag{23}$$

Combining the energy and Gibbs equations,

$$q'\,dx = \dot{m}(T\,ds + v'''\,dp) - \left(\frac{i_y^2}{\sigma}\right)4ab\,dx \tag{24}$$

Then, using the entropy equation,

$$q'\,dx = T\left(d\dot{P}_s + \frac{q'dx}{T+\Delta T}\right) + \dot{m}\,\frac{dp}{\rho} - \left(\frac{i_y^2}{\sigma}\right)4ab\,dx \tag{25}$$

which can be re-arranged as follows:

$$\frac{d\dot{P}_s}{dx} = \frac{q'}{T} - \frac{q'}{T+\Delta T} - \frac{\dot{m}}{\rho T}\frac{dp}{dx} + 4ab\frac{i_y^2}{\sigma T} \tag{26}$$

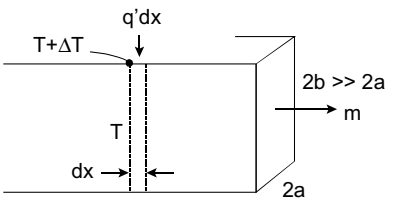

Fig. 2. Schematic of heat and mass flow in a microchannel.

This result gives the rate of change of entropy production in the streamwise (x) direction of the microchannel. This result requires spatial integration to yield the local rate of entropy production at each x-position.

Alternatively, the entropy production rate can be expressed as a sum of positive-definite terms corresponding to friction, thermal and electromagnetic irreversibilities, i.e.,

$$\dot{P}_s = \frac{k\nabla T\cdot\nabla T}{T^2} + \frac{\mu\Phi}{T} + \frac{\sigma_e}{T}(\vec{E}+\vec{v}\times\vec{B})\cdot(\vec{E}+\vec{v}\times\vec{B}) \tag{27}$$

In Eq. (26), the terms on the right side represent a sum of squared terms, so the entropy production is positive, thereby complying with the Second Law of Thermodynamics.

Based on the assumptions outlined previously in the fluid flow and heat transfer formulations, it can be shown that the reduced form of the entropy production equation can be written as

$$\dot{P}_s = \frac{k}{T^2}\left(\frac{dT}{dz}\right)^2 + \frac{\mu}{T}\left(\frac{du}{dz}\right)^2 + \frac{i_y^2}{\sigma_e T} \tag{28}$$

Define the following non-dimensional entropy production, $\dot{P}_s^*$, and wall temperature,

$$\dot{P}_s^* = \frac{\dot{P}_s}{k/a^2} \tag{29}$$

$$\theta_w = \frac{kT_w}{\mu u_b^2} \tag{30}$$

Using these variables, the non-dimensional entropy production equation becomes

$$\dot{P}_s^* = \frac{(d\theta/dz^*)^2}{(\theta+\theta_w)^2} + \frac{(du/dz^*)^2}{\theta+\theta_w} + \frac{i_y^{*2}}{\theta+\theta_w} \tag{31}$$

Three cases will be considered, namely (i) frictional exergy losses and combined frictional/thermomagnetic exergy losses, subject to (ii) constant wall temperature and (iii) constant wall heat flux conditions.

4.1. Case (i): Frictional exergy losses in channel flow

The previous expressions of entropy production and exergy losses include friction and thermomagnetic irreversibilities. The former component due to friction will be validated separately. For incompressible, fully-developed flow within a channel of length L and width of $2a$, the velocity profile is given by the well-known Poiseuille flow solution, i.e.,

$$u(z) = \frac{a^2\Delta p}{2\mu L}\left[\left(\frac{z}{a}\right)^2 - 1\right] \tag{32}$$

Differentiating with respect to z to find the entropy production rate and multiplying by temperature yields the following ratio of exergy destruction to maximum exergy destruction (at the wall),

$$\frac{\dot{X}_{\mathrm{d}}}{\dot{X}_{\mathrm{d,w}}} = \left(\frac{z}{a}\right)^2 \tag{33}$$

This result indicates that the exergy destruction ratio is minimum (zero) along the center line.

4.2. Case (ii): Combined friction/thermomagnetic exergy loss (constant wall temperature)

In this case, the thermal boundary conditions are given by

$$\theta(\pm 1) = 0 \tag{34}$$

Solving the internal energy equation subject to these boundary conditions, it can be shown that

$$\theta = \frac{M^2}{(M\cosh M - \sinh M)^2}\left[\frac{C^2}{2}(1 - z^{*2}) + \frac{2C}{M}(\cosh M - \cosh Mz^*) + \frac{1}{4}(\cosh 2M - \cosh 2Mz^*)\right] \tag{35}$$

This result confirms that both the Hartmann number and load factor affect the temperature profile.

Then, the entropy production at the wall can be determined after differentiating the temperature profile and evaluating the spatial derivatives at the wall ($z^* = 1$). Furthermore, Ohm's Law is used to express the current density in terms of the load factor, thereby yielding the following result for the rate of exergy destruction at the wall,

$$\dot{X}^*_{\mathrm{d,w}} = \theta_{\mathrm{w}}\dot{P}^*_{s,w} = \left(\frac{M}{M\cosh M - \sinh M}\right)^4 \times \left(C^2 + 2C\sinh M + \frac{M}{2}\sinh 2M\right)^2 \frac{1}{\theta_{\mathrm{w}}} + \left(\frac{M^2\cosh M}{M\cosh M - \sinh M}\right)^2 + M^2\left(K - M\frac{\cosh M - \sinh M}{M\cosh M - \sinh M}\right)^2 \tag{36}$$

4.3. Case (iii): Combined friction/thermomagnetic exergy loss (uniform wall heat flux)

In this case, the thermal boundary conditions are given by

$$\theta(1) = 0 \tag{37}$$

$$\left.\frac{\mathrm{d}\theta}{\mathrm{d}z^*}\right|_1 = q^*_{\mathrm{w}} \tag{38}$$

where the non-dimensional wall heat flux is given by the following expression,

$$q^*_{\mathrm{w}} = \frac{q''_{\mathrm{w}}}{\mu u_{\mathrm{b}}^2/a} \tag{39}$$

In this case, the right wall temperature is unknown and the temperature profile is assumed to be symmetric about the mid-plane of the microchannel. Due to symmetry, only the right half-channel is considered in the analysis.

Solving the internal energy equation subject to the previous boundary conditions,

$$\theta(z^*) = q^*_{\mathrm{w}}\frac{2C^2(z^{*2} - 1) + 8C(\cosh Mz^* - \cosh M)/M}{4C^2 + 8C\sinh M + 2M\sinh 2M} + q^*_{\mathrm{w}}\frac{(\cosh 2Mz^* - \cosh 2M)}{4C^2 + 8C\sinh M + 2M\sinh 2M} \tag{40}$$

It can be verified that this result is symmetrical about the mid-plane of the microchannel. Using this result, the non-dimensional rate of exergy destruction at the wall becomes

$$\dot{X}^*_{\mathrm{d,w}} = \frac{q^{*2}_{\mathrm{w}}}{\theta_{\mathrm{w}}} + \left(\frac{M^2\cosh M}{M\cosh M - \sinh M}\right)^2 + M^2\left(K - M\frac{\cosh M - \sinh M}{M\cosh M - \sinh M}\right)^2 \tag{41}$$

For large Hartmann numbers, the exponential e^{-M} becomes much less than e^{M}, so the exergy destruction at the wall can be simplified as follows:

$$\dot{X}^*_{\mathrm{d,w}} = \frac{q^{*2}_{\mathrm{w}}}{\theta_{\mathrm{w}}}\left(\frac{\mu u_{\mathrm{b}}^2}{kT_{\mathrm{w}}}\right)^2 + \frac{M^4}{(M-1)^2} + M^2K^2 \tag{42}$$

Exergy losses have important implications regarding the performance of microdevices. For energy consuming systems, such as input power needed for electrically driven flow in microchannels, exergy destruction characterizes dissipative losses leading to reduced system efficiency. On the other hand, recent advances involving micro energy sources, such as micro heat engines [23], involve power generation. In this case, exergy losses represent a portion of energy which may have been converted to useful work, but was lost through friction and thermomagnetic irreversibilities. In the following sections, the previous results of exergy destruction will be used for optimization purposes.

5. Minimization of exergy losses

Re-arranging Eq. (42) in terms of the Reynolds number (Re), magnetic Prandtl number (Pr_m) and thermo-magnetic number (N),

$$\dot{X}^*_{d,w} = \frac{1}{4\theta_w}\left(\frac{q'_w \dot{m}^2 \rho^2}{16\beta^3\mu^5}\right)^2 Re^{-8} + \theta_w N(1+K^2)Pr_m^2 Re^2 \quad (43)$$

where

$$Re = \frac{\rho u_b a}{\mu} \quad (44)$$

$$Pr_m = \frac{\mu\mu_e\sigma_e}{\rho} \quad (45)$$

$$N = \frac{H_e^2}{\sigma_e k T_w} \quad (46)$$

and μ_e and H_e are the magnetic permeability and electric field strength, respectively. Also, β and q'_w are the micro-channel aspect ratio (b/a) and wall heat flux per unit length of microchannel.

Differentiating the expression for exergy destruction with respect to the Reynolds number and setting the result equal to zero yields the following optimal Reynolds number,

$$Re_{L,opt} = \frac{0.574B^{1/5}}{\left[N(1+K^2)\beta^6\right]^{1/10}} \quad (47)$$

where the duty parameter, B, is given by

$$B = \frac{q'\dot{m}^2\rho^2}{Pr_m\mu^5\theta_w} \quad (48)$$

At this optimum, the least input power is needed to transfer fixed rates of mass and heat flow through the microchannel.

6. Experimental study of exergy losses in channel flow

Experimental studies of friction and thermal irreversibilities (not electromagnetic irreversibilities) were performed for validation of limiting cases of predicted exergy losses. Channel flow was studied in a water tunnel with pulsed laser PIV (particle image velocimetry) and 5 μm diameter polyamide seeding particles (see Fig. 3). The parallel channel is 12.6 mm high, 60 cm wide and 2 m long. The height does not represent a microchannel. However, pulsed laser measurements were obtained within close proximity of the wall (within 0.2 mm from the wall) and both configurations have diffusion dominated transport near the wall. Also, dynamic similarity between the configurations occurs at an equivalent Reynolds number, so the measurements were considered to provide useful data for validation of the theoretical modeling.

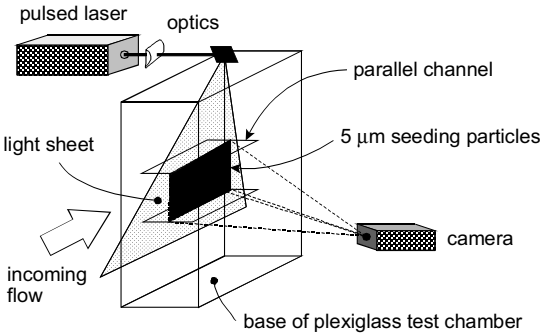

Fig. 3. Schematic of pulsed laser and PIV measurements.

In the experimental setup, a Dantec 2100 PIV system, reflecting optics, two-chamber Gemini PIV Nd: Yag pulsed laser and HiSense CCD camera were used. The pulsed laser illuminated a planar cross-section in the center of the channel, perpendicular to the wall. Camera images of illuminated particles at two different times were processed, matched and sub-divided into interrogation regions to determine the displacement of a group of particles (based on FFT correlation techniques). The fluid velocities were determined from these digital images, after dividing the distance by the elapsed time of laser pulses.

When collecting the experimental data, a procedure for optimizing the time between laser pulses was needed for establishing the particle seeding density. The PIV peak height ratio and velocity length sliders were adjusted, so any vectors longer than a specified portion of length within the interrogation area were highlighted in red (i.e., considered inaccurate). Starting with a low time between pulses and gradually increasing the time between successive images, the velocities in the vector map became sufficiently smooth and continuous. This time was increased until red vectors appeared, at which point the optimum time between laser pulses was determined. The duration of the pulses was 0.01 μs. The camera focus was adjusted until outlier vectors from successive images were minimized to a few large outlier vectors. In the PIV experiments, if more outliers occurred and they could not be removed after focus adjustments of the camera, then more seeding particles were added. A minimum of five particles per interrogation cell was needed for cross-correlation of the measured data.

The Dantec PIV system permitted other adjustable cross-correlation parameters in the experimental procedure. A specified overlap percentage of interrogation areas was used in the PIV software, in order to allow sufficient over-sampling of the flow field. Additionally, moving-average validations allowed vectors to be rejected based on a comparison between neighboring vectors and replacement of vectors with surrounding values. The moving-average filter replaced each vector

with a weighted average of neighboring vectors. This process reduces errors arising from amplification of noise in the signal received by the PIV system. Sufficient statistical averaging of vector maps was performed, until the number of averaged readings did not appear to have appreciable effects on the spatial velocity field. After fluid velocities were measured over the discrete PIV grid, the data were post-processed to derive friction irreversibilities and exergy destruction, based on the viscous dissipation divided by temperature. Additional details regarding these procedures have been documented previously [24]. The maximum error of measured exergy destruction was estimated to be about 11.67% near the wall, but the measured data are generally considered to be accurate within $\pm 6.6\%$ away from the wall (see Appendix A). In addition to whole-field PIV, this method can be applied to other measurement techniques, such as LDA or PDA.

7. Results and discussion

In this section, predicted results will be compared against measured data and computational simulations with a finite element/volume formulation, which has been documented and validated in previous work [25]. Detailed information regarding numerical modeling and validation of the computational formulation is outlined in Ref. [25]. Furthermore, the predicted results will be presented and compared against past data reported by Bejan [18], Salas et al. [26] and Adeyinka and Naterer [27]. The predicted results will be presented in terms of non-dimensional variables described in previous sections. In particular, these non-dimensional variables include the cross-stream coordinate ($z^* = z/a$), velocity ($u^* = u/u_b$), Hartmann number (M), temperature (θ), Reynolds number (Re), load factor (K) and duty parameter (B).

In Fig. 4, the predicted non-dimensional temperature is shown at varying Hartmann numbers and load factors. It can be observed that the temperature and near-wall temperature gradient decrease at lower Hartmann numbers. Also, they decrease with larger load factors. The load factor (K) represents the ratio of the applied electric field strength to the product of the mean velocity and magnetic field strength. The electromagnetic resistance of fluid motion decreases at larger load factors, when the magnetic field strength decreases. As a result, the fluid velocity increases in the denominator of the non-dimensional temperature, thereby reducing the temperature of the fluid. As expected, the temperature decreases when the wall heating rate is reduced (see Fig. 5).

Exergy destruction within the microchannel occurs from both friction and thermomagnetic irreversibilities. Each component can be isolated, in order to assess the varying roles of fluid friction, heat exchange and electromagnetic forces on energy conversion within the microchannel. In Fig. 6, the frictional component is isolated and the ratio of local exergy destruction to the maximum exergy destruction (at the wall) is plotted. Close

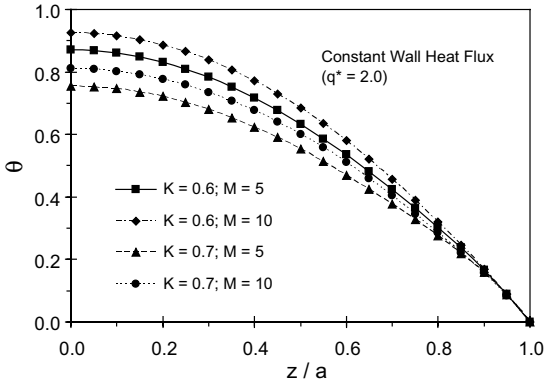

Fig. 4. Non-dimensional temperature at varying Hartmann numbers.

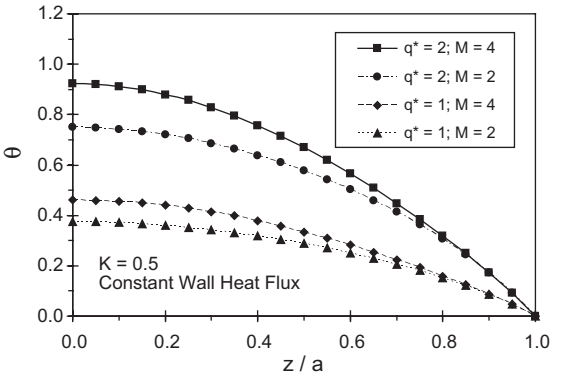

Fig. 5. Temperature profiles at varying wall heating rates.

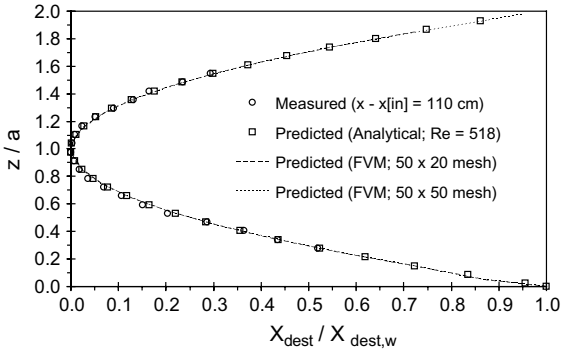

Fig. 6. Comparison of predicted exergy destruction and measured data.

agreement is achieved between analytical, computational and measured results. This close agreement provided useful validation of the theoretical modeling of the frictional component of exergy losses.

The flow configuration and experimental method were described in section V. Computational simulations were performed with a FVM (finite volume method), which has been documented previously and validated in Ref. [25]. In Fig. 6, measurements were recorded at a distance of 110 cm downstream of the inlet of the channel. At this point, the fluid motion was fully developed. Although the channel height (12.6 mm), Reynolds number (518) and closest measurement to the wall (0.2 mm) do not match the microchannel problem, the frictional exergy destruction occurs from the same component in both configurations (second term on right side of Eq. (31)). As a result, the comparison against measured data in Fig. 6 provides a useful validation of frictional exergy losses of fluid transport in channels. Also, the measurements provide a useful basis from which future developments could include the additional thermomagnetic irreversibilities. For example, planar laser induced fluorescence (PLIF) could be applied in a similar manner to whole-field measurements of thermal irreversibilities.

In Fig. 7, the rate of exergy destruction is illustrated for a microchannel half-width of 43 μm, load factor of 0.5, Hartmann number of 20 and varying magnetic field strengths. It can be observed that exergy destruction decreases at lower magnetic field strengths, due to lower electromagnetic irreversibilities. Also, the exergy destruction reaches a peak value at the wall. Then, it decreases to a local minimum and rises to a uniform non-zero value in the core of the microchannel. The exergy destruction approaches zero at the mid-plane in Fig. 6, as electromagnetic irreversibilities were not included in the exergy destruction. But these irreversibilities are included in Fig. 7 and they increase towards the mid-plane of the microchannel, thereby yielding a non-zero exergy destruction in the mid-plane. From Ohm's Law, the electromagnetic irreversibility is proportional to the velocity squared, so the point of maximum electromagnetic irreversibility occurs at the mid-plane ($z^* = 0$).

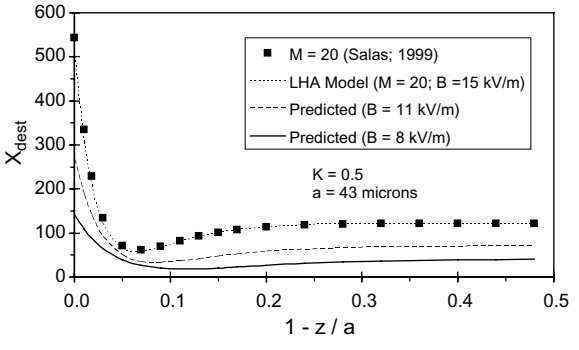

Fig. 7. Entropy generation with varying magnetic field strength.

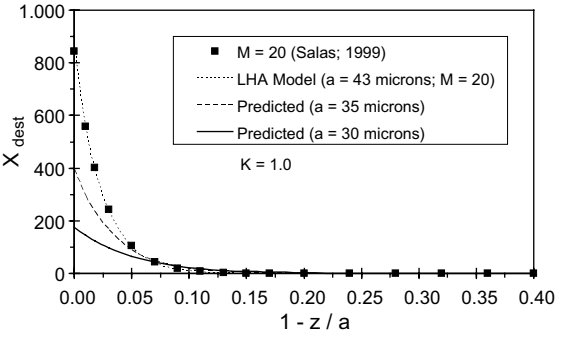

Fig. 8. Exergy destruction for various microchannel sizes.

The exergy destruction increases for wider microchannels (see Fig. 8), since added surface area increases the friction irreversibilities. The electromagnetic irreversibility decreases at higher load factors, due to a lower magnetic field strength. As a result, the higher load factor of $K = 1.0$ in Fig. 8 yields a monotonically decreasing exergy destruction towards zero in the mid-plane of the microchannel, without a local minimum and rising trend observed in Fig. 7. The results in Figs. 7–9 indicate the friction irreversibility is highest near the walls, while the electromagnetic irreversibility is dominant within the core of the microchannel. If the fluid friction is sufficiently small at low Reynolds numbers and the Hartmann number is sufficiently large, the maximum exergy destruction may occur at the mid-plane. Unlike classical problems involving convective heat transfer without electromagnetic forces, the point of maximum exergy destruction may not be located at the wall. As a result, local loss coefficients may be better represented in terms of local exergy

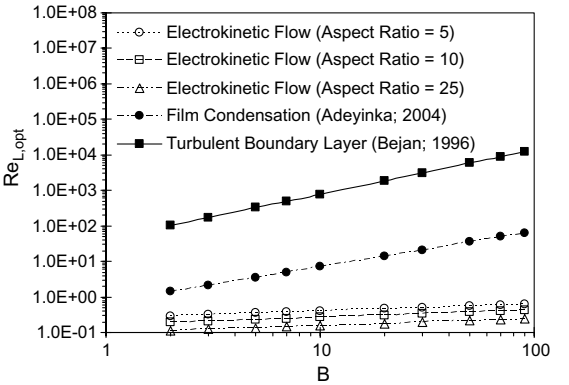

Fig. 9. Optimal Reynolds number at varying magnetic field strengths.

destruction, rather than friction coefficients at the wall, which may not best reflect the most relevant location of dissipative losses in electrohydrodynamic flows.

It should be noted that the predicted results are determined from the LDA model in Figs. 7 and 8. At different values of z/a, the trends of exergy destruction in the predicted results show close agreement with Salas's data (1999) at the same Hartmann number ($M = 20$). Those comparisons are shown at the same Hartmann number for validation purposes. Additional sensitivity studies at other Hartmann numbers are also shown in the same figures. For example, lower magnetic field strengths ($B = 11$ and 8 kV/m) are shown in Fig. 7, which correspond to different Hartmann numbers. As a result, those sensitivity studies cannot be compared directly to Salas's data (1999), since the Hartmann numbers are not equivalent. Nevertheless, the additional sensitivity studies provide useful insight regarding trends at varying strengths of the applied magnetic field. For example, when the value of B decreases below $B = 15$ kV/m in Fig. 7 (corresponding to the case of $M = 20$), the trends of exergy destruction are different than Salas's data (1999) at different values of z/a, since the electromagnetic irreversibility decreases at lower values of the magnetic field strength. At the center of the channel, the exergy destruction for $B = 8$ kV/m is about 67% lower than the case with $B = 15$ kV/m, as the Hartmann number decreases by about 47% so the electromagnetic irreversibility decreases accordingly.

In Fig. 9, the optimal Reynolds number, $Re_{L,opt}$, which minimizes the net exergy destruction, is plotted at varying duty parameters, aspect ratios and flow configurations (turbulent boundary layer [18]; film condensation [27]). The optimum is lower than other configurations [18,27] and it increases at higher duty parameters and smaller aspect ratios. This optimum involves a certain balance, which minimizes the net exergy destruction arising from combined effects of friction and thermomagnetic irreversibilities. The friction irreversibility is reduced with a smaller surface area and net friction, but higher thermal irreversibilities occur due to a higher temperature difference (between fluid and wall) needed to transfer a specified heat flow (q) over a smaller area. However, the thermal irreversibility decreases with a larger surface area, since a smaller temperature difference between the fluid and wall is needed to transfer the fixed heat flow. This reduction comes at the expense of higher friction irreversibilities, when the larger surface area (i.e., larger Reynolds number) contributes to added surface friction. Furthermore, the electromagnetic irreversibility increases at higher Reynolds numbers, since Ohm's Law outlines that this irreversibility is proportional to the velocity squared. These varying trends contribute to the physical mechanisms which minimize the net rate of exergy destruction at $Re_{L,opt}$.

The previous results of exergy destruction have practical significance in electrically driven flow in microchannels. These exergy losses characterize the friction, pressure losses and kinetic energy dissipated to internal energy within the microchannel. As a result, they have an important role in the performance of microdevices. For example, consider cooling of an electronic assembly with microchannels. Each unit of exergy destroyed represents an amount of internal energy, which could have been removed by convective cooling, but was not removed due to energy dissipated internally by the thermomagnetic irreversibilities. Additional power input is needed to offset these irreversibilities. As future microdevice technologies become more complex in terms of energy conversion between various sub-systems, it is anticipated that tracking of exergy losses throughout these networks will become an increasingly useful tool in reaching the technological goals therein.

8. Conclusions

This article considers exergy losses of electrohydrodynamic flow in microchannels. Friction, thermal and electromagnetic irreversibilities contribute to exergy destruction, which leads to additional input power required to deliver fixed rates of mass flow and heat exchange within the microchannel. This input power is supplied to manipulate the electric charge pattern along the walls, thereby generating forces that control the speed and direction of fluid motion. In this article, predicted velocity and temperature profiles are post-processed to find local rates of exergy destruction within the microchannel. Also, non-intrusive measurements of whole-field exergy destruction are presented. Theoretical predictions are validated through comparisons with this measured data and other past data. Unlike Poiseuille flow, the predicted results show non-zero entropy production in the core of the microchannel for electrohydrodynamic flows, due to the rising electromagnetic irreversibilities. It is shown that the optimal Reynolds number (minimizing the exergy destruction) increases at smaller aspect ratios of the microchannel. Less surface area leads to higher thermal irreversibilities below the optimum, as a larger temperature difference (between fluid and wall) is needed to transfer a fixed rate of heat flow. The load factor of the electric circuit appears to have minor impact on the optimum. The results show how exergy losses have importance in effective flow control in microchannels.

Acknowledgement

Support of the microfluidics research from the Natural Sciences and Engineering Research Council of Can-

ada, Manitoba Hydro (Canada) and the Canada Foundation for Innovation are gratefully acknowledged.

Appendix A. Measurement uncertainties

A measurement uncertainty analysis of PIV measurements was performed based on the AIAA standard [28]. The total error is a sum of the bias component, B, and a precision component, P. For the measured velocity, U, its bias error is related to the elementary bias errors as follows:

$$B_U^2 = \eta_{\Delta s}^2 B_{\Delta s}^2 + \eta_{\Delta t}^2 B_{\Delta t}^2 + \eta_{L_o}^2 B_{L_o}^2 + \eta_{L_I}^2 B_{L_I}^2 \quad (A.1)$$

where the sensitivity coefficients are defined as $\eta_\chi = \partial U/\partial\chi$. Also, Δt is the time interval between laser pulses, Δs is the particle displacement from the correlation algorithm, L_o is the width of the camera view in the object plane and L_I is the width of the digital image. Using the manufacturer's specifications of the elementary bias limits and combining the contributions of each bias error and the sensitivity coefficient, a velocity error of 0.76% was obtained.

Furthermore, the precision error (P) for measurements of N samples is given by

$$P = \frac{t\sigma}{N} \quad (A.2)$$

where t is the confidence coefficient (equaling 2 for a 95% confidence interval) and σ is the standard deviation of the sample of N images. Values of the standard deviation along the center line and the near-wall region were calculated to be 15% and 33%, respectively. These values yielded precision limits of 0.67% and 1.55% for those regions. Thus, the total uncertainties of measured velocity in the mid-plane and near-wall regions become 1.4% and 2.2%, respectively.

Using these velocity results, the measurement error of exergy destruction, X_d, can be estimated based on the following data reduction equation for fully developed flow,

$$X_d = \mu\left(\frac{\Delta u}{\Delta y}\right)^2 + k\left(\frac{\Delta T}{\Delta y}\right)^2 \quad (A.3)$$

A similar procedure is performed with bias and precision errors involving exergy destruction. As a result, the total error becomes

$$\varepsilon_{P_s}^2 = \eta_T^2\varepsilon_T^2 + \eta_{\Delta U}^2\varepsilon_{\Delta U}^2 + \eta_{\Delta y}^2\varepsilon_{\Delta y}^2 + \eta_{\Delta T}^2\varepsilon_{\Delta T}^2 \quad (A.4)$$

The maximum total uncertainty of exergy destruction was estimated to be about 11.67% at a point of 3 mm from the bottom wall. This uncertainty represents the maximum error bound within a 95% confidence interval. Additional comparisons between measured and analytical results within the channel show less error closer to the center-line of the channel.

References

[1] M. Gad-el-Hak, The fluid mechanics of microdevices—the freeman scholar lecture, ASME J. Fluids Eng. 121 (March) (1999) 5–33.
[2] G.F. Naterer, Surface micro-profiling for reduced energy dissipation and exergy loss in convective heat transfer, Microscale Thermophys. Eng. 9 (3) (2005), to appear.
[3] G.F. Naterer, Adaptive surface micro-profiling for microfluidic energy conversion, AIAA J. Thermophys. Heat Transfer 18 (4) (2004) 494–501.
[4] G.F. Naterer, S.R. Chomokovski, C. Friesen, C. Shafai, Micro-machined Surface Channels Applied to Engine Intake Flow and Heat Transfer, AIAA Paper 2003-4054, AIAA 36th Thermophysics Conference, Orlando, FL, 23–26 June 2003.
[5] B. Zhao, J.S. Moore, D.J. Beebe, Surface-directed liquid flow inside microchannels, Science 291 (5506) (2001) 1023–1026.
[6] E.Y.K. Ng, S.T. Tan, Computation of three-dimensional developing pressure-driven liquid flow in a microchannel with EDL effect, Numer. Heat Transfer: Part A: Appl. 45 (10) (2004) 1013–1027.
[7] S.K. Cho, H. Moon, C.J. Kim, Creating, Transporting, cutting and merging liquid droplets by electrowetting based actuation for digital microfluidic circuits, J. Microelectromech. Syst. 12 (2003) 70–80.
[8] J.N. Israelachvili, Measurement of the viscosity of liquids in very thin films, J. Colloid Interf. Sci. 11 (1) (1986) 263–271.
[9] N.P. Migun, P.P. Prokhorenko, Measurement of the viscosity of polar liquids in microcapillaries, Colloid J. USSR 49 (5) (1987) 894–897.
[10] J.L. Anderson, J.A. Quinn, Ionic mobility in microcapillaries, Faraday Trans. I 68 (1972) 744–748.
[11] J. Ferziger, H.G. Kaper, Mathematical Theory of Transport Processes in Gases, North-Holland Publishing Company, London, 1972.
[12] J. Avsec, Calculation of transport coefficients of R-32 and R-125 with the methods of statistical thermodynamics and kinetic theories of gas, Arch. Thermodyn. 24 (3) (2003) 69–82.
[13] J. Avsec, Calculation of equilibrium and nonequilibrium thermophysical properties by means of statistical mechanics, J. Tech. Phys. 44 (2003) 1–17.
[14] J. Pfahler, J. Harley, H. Bau, Liquid transport in micron and submicron channels, Sensors Actuators A21–A23 (1990) 431–434.
[15] J. Pfahler, J. Harley, H. Bau, J.N. Zemel, Gas and liquid flow in small channels, Symp. Microelectromech. Sensors Actuators Syst. 32 (1991) 49–60.
[16] G.F. Naterer, Establishing heat–entropy analogies for interface tracking in phase change heat transfer with fluid flow, Int. J. Heat Mass Transfer 44 (15) (2001) 2903–2916.
[17] G.F. Naterer, Applying heat–entropy analogies with experimental study of interface tracking in phase change heat transfer, Int. J. Heat Mass Transfer 44 (15) (2001) 2917–2932.
[18] A. Bejan, Entropy Generation Minimization, CRC Press, Boca Raton, FL, 1996.

[19] G.F. Naterer, Heat Transfer in Single and Multiphase Systems, Section 5.4.3, CRC Press, Boca Raton, FL, 2002.
[20] G.F. Naterer, J.A. Camberos, Entropy and the second law in fluid flow and heat transfer simulation, AIAA J. Thermophys. Heat Transfer 17 (3) (2003) 360–371.
[21] J.A. Camberos, Quantifying irreversible losses for magnetohydrodynamic (MHD) flow simulation, AIAA Paper 2003-3647, AIAA 36th Thermophysics Conference, Orlando, FL, 23–26 June, 2003.
[22] J.A. Camberos, On the construction of exergy balance equations for availability analyses, AIAA Paper 2002-2880, AIAA/ASME 8th Joint Thermophysics Conference, St. Louis, MO, 24–27 June, 2002.
[23] S. Whalen, M. Thompson, D. Bahr, C. Richards, R. Richards, Design, fabrication and testing of the P3 micro heat engine, Sensors Actuators 104 (2003) 200–208.
[24] O.B. Adeyinka, G.F. Naterer, A new second law based loss mapping with PIV for turbulent flows, 11th International Symposium on Flow Visualization, Notre Dame, IN, 9–12 August, 2004.
[25] O.B. Adeyinka, G.F. Naterer, Apparent entropy production difference with heat and fluid flow irreversibilities, Numer. Heat Transfer B 42 (5) (2002) 411–436.
[26] H. Salas, S. Cuevas, M.L. de Haro, Entropy generation analysis of magnetohydrodynamic induction devices, J. Phys. D: Appl. Phys. 32 (1999) 2605–2608.
[27] O.B. Adeyinka, G.F. Naterer, Optimization correlation for entropy production and energy availability in film condensation, Int. Commun. Heat Mass Transfer 31 (4) (2004) 513–524.
[28] AIAA Standard S-071-1995, Assessment of Experimental Uncertainty with Application to Wind Tunnel Testing, American Institute of Aeronautics and Astronautics, Washington, DC, 1995.